Modeling dilute sediment suspension using large-eddy simulation with a dynamic mixed model

Yi-Ju Chou[a)] and Oliver B. Fringer
Environmental Fluid Mechanics Laboratory, Stanford University, Stanford, California 94305, USA

(Received 29 April 2008; accepted 28 August 2008; published online 12 November 2008)

Transport of suspended sediment in high Reynolds number channel flows [Re=O(600 000)] is simulated using large-eddy simulation along with a dynamic-mixed model (DMM). Because the modeled sediment concentration is low and the bulk Stokes' number (St_b) is small during the simulation, the sediment concentration is calculated through the use of the Eulerian approach. In order to employ the DMM for the suspended sediment, we formulate a generalized bottom boundary condition in a finite-volume formulation that accounts for sediment flux from the bed without requiring specific details of the underlying turbulence model. This enables the use of the pickup function without requiring any assumptions about the behavior of the eddy viscosity. Using our new boundary condition, simulations indicate that the resolved component of the vertical flux is one order of magnitude greater than the resolved subfilter-scale flux, which is in turn one order of magnitude greater than the eddy-diffusive flux. Analysis of the behavior of the suspended sediment above the bed indicates the existence of three basic time scales that arise due to varying degrees of competition between the upward turbulent flux and downward settling flux. Instantaneous sediment concentration and velocity fields indicate that streamwise vortices account for a bulk of the resolved flux of sediment from the bed. © *2008 American Institute of Physics*. [DOI: 10.1063/1.3005863]

I. INTRODUCTION

Numerous laboratory and field studies document the complex physics of suspended sediment and its relationship to bedform dynamics. However, uncertainties and difficulties arise for turbulent flow, particularly for high Reynolds number field-scale flows. Entrainment and suspension of suspended sediment and its transport in the water column are highly correlated with turbulent features, particularly near the bottom. Therefore, interactions between sediment transport and turbulence are very important, and a model to study these mechanisms must have the capability to couple them in an accurate manner. Owing to advances in computer power, numerical simulation has become a powerful tool in studying the sediment transport problem with high resolution. Depending on the treatment of sediment, models are based on either one of two approaches: the Lagrangian particle tracking approach, which tracks individual particles in the flow, and the Eulerian continuum approach, which treats sediment as a continuous scalar field and is concerned with its concentration at fixed points. In general, the Lagrangian particle tracking approach, which allows either one-way coupling (only flow affects particles) or two-way coupling (particle-flow interactions), has been successfully applied to particle-laden flows, and detailed observations of particle motions have been achieved.[1–6] However, because the motion of each particle must be computed at each time step, the Lagrangian approach may not be practical for the study of fine sediment suspensions. Although it has been employed to study such problems, due to its restrictively high computational loading, only small-scale features close to the bed, or so-called bedload, can be observed.[7–10] The alternative of sediment suspension simulation is to employ the Eulerian approach. Due to the assumption that particles follow the fluid motion and particle-fluid interactions are neglected, the Eulerian approach is also a method of one-way coupling. This approach has been successfully applied to different sediment transport problems for laboratory-[11–13] and field-scale[14] flows.

This study focuses on entrainment of sediment from the channel bed and its further transport in the water column in a turbulent channel flow. In the past decade, great attention has been paid to particle-laden flow, and most related studies have focused on transport of a finite number of particles in isotropic and homogeneous turbulent flow (e.g., Refs. 2–4 and 6). Through numerical simulation, interactions between turbulence and particles have been studied extensively in these works, but suspension of a large number of sediment particles due to turbulence is still not well understood. While particle entrainment and its further suspension in turbulent flow is a common phenomenon in the natural environment, it is not common to see homogeneous and isotropic turbulence in geophysical flows, where strong turbulence is usually associated with the free-stream velocity field, e.g., in rivers and coastal flows. Thus, in order to study the properties of sediment suspension in water, the major difference between this study and other particle-laden flow-related studies is that in this study, we have unlimited sediment pickup from the channel bed. Since it is impossible to resolve all of the scales of strong turbulence in this study, fine-scale particle physics in turbulent flow is ignored, such as preferential accumulation[3,4,6] and turbophoresis,[1,5,15] which may enhance the particle momentum. According to Bosse *et al.*,[6] the mechanism responsible for the particle velocity enhancement

[a)]Electronic mail: yjchou@stanford.edu.

can be explained as a result of three mechanisms: (1) the inertial bias by which the particles accumulate in regions of high strain rate and low vorticity; (2) the preferential sweeping in the presence of gravity; (3) the local modification of the fluid velocity structure by the particles in regions of increased particle volume fraction. The first and second contributions are those associated with small-scale turbulent features, e.g., the streamwise vortex cores in the boundary layer. The third can only be simulated using two-way coupling, and in our study it is likely significant near the channel bed, where high concentrations may occur. Although these phenomena can be important in sediment suspension, especially near the bottom, it is difficult to simulate these processes in the presence of high Reynolds number turbulent flow. In this study, due to the small particle time scale $[t_b = O(10^{-5})\ \mathrm{s}]$ compared to the simulation time step ($\Delta t = 0.005$ s), it is assumed that the particles follow the flow and do not have separate dynamics other than gravitational settling. Therefore, the Eulerian approach with the present bottom boundary condition is employed to simulate sediment transport, which ignores fine-scale physics and focuses on sediment transport due to resolved turbulent eddies.

The most critical issue with regard to using the scalar transport equation for modeling sediment suspension is the sediment boundary condition at the bed.[16] From a physical point of view, sediment is entrained into the water column when the shear stress is higher than the critical value. Therefore, in the sediment model, the bottom boundary condition must represent the sediment entrainment resulting from the excess shear stress. Numerous laboratory experiments have been conducted to obtain "reference concentration" formulae to prescribe the near-bed concentration at the reference level.[17–19] These results have proved very useful for employing Dirichlet boundary conditions for the sediment concentration. However, the reference concentration formulae are obtained for flows in equilibrium and may not be suitable for unsteady flows. Furthermore, as suggested by van Rijn,[20] the model results are quite sensitive to the parameter setup, particularly the reference level. An alternative approach is to use the pickup function, which has been suggested by Nielsen[21] as a proper approach to model unsteady sediment transport. This approach has been used by Zedler and Street[12,13] to model sediment suspension using large-eddy simulation (LES) in both steady and oscillatory flows.

The bottom boundary condition for the suspended sediment in the simulations of Zedler and Street[12,13] is given by

$$\frac{\nu_T}{\mathrm{Pr}_T}\frac{\partial \bar{C}}{\partial z} = -P_k, \tag{1}$$

where ν_T is the eddy viscosity, Pr_T is the turbulent Prandtl number, $\bar{C}$ is the grid-filtered sediment concentration (in a LES framework), z represents the vertical direction, and P_k is the pickup function. The same formula was employed by van Rijn[22] with a parabolic eddy-viscosity model. However, this boundary condition is highly restricted by the magnitude of the eddy viscosity at the bottom since a small-eddy viscosity can result in an unrealistically high concentration gradient.

The aforementioned simulations of suspended sediment concentration employ a parabolic eddy-viscosity model in order to yield correct near-wall behavior of the velocity field. Depending on the LES implementation, the eddy viscosity may or may not be an important contributor to the overall turbulent stress, and excessively high near-bed sediment concentration gradients may result when it is small. For example, when the dynamic-mixed model (DMM) for the subfilter-scale (SFS) motions[23] is employed, the turbulent flux due to the eddy viscosity may be negligible, particularly near the bed. In this paper we present a formulation that eliminates the drawbacks associated with small near-bed eddy viscosities by implementing a new boundary condition in which the sediment entrainment is induced not only by turbulent diffusion, but by all of the components of the subgrid-scale stress tensor in the LES formulation. This approach is developed from first principles in a finite-volume context and, as demonstrated in Sec. II, is a general formulation for the bottom boundary condition that can be applied to a variety of turbulence models when using the Eulerian approach.

The rest of this paper is organized as follows: In Sec. II, we derive the bottom boundary condition for both the fluid and the suspended sediment using the finite-volume approach. In Sec. III, the boundary condition is further derived for the implementation in LES with DMM, and we describe the setup of the numerical simulations in detail. In Sec. IV, results from both transient and statistically steady states are discussed, and conclusions are drawn in Sec. V.

II. MATHEMATICAL FORMULATION

The unsteady, three-dimensional motion of an incompressible fluid with constant density is described by

$$\frac{\partial u_j}{\partial x_j} = 0, \tag{2}$$

$$\frac{\partial u_i}{\partial t} + \frac{\partial (u_i u_j)}{\partial x_j} = -\frac{1}{\rho}\frac{\partial p}{\partial x_j}\delta_{ij} + \nu\frac{\partial^2 u_i}{\partial x_j\,\partial x_j}, \tag{3}$$

where the scalar transport equation for suspended sediment is given by

$$\frac{\partial C}{\partial t} + \frac{\partial}{\partial x_j}[(u_j - w_s\delta_{j3})C] = 0. \tag{4}$$

The Einstein summation convention and notation are assumed, and t is the time, x_j is the Cartesian coordinate, u_j is the velocity, ρ is the density of water, ν is the kinematic viscosity, p is the pressure, and w_s is the sediment settling velocity, which is the terminal velocity of a particle in the fluid at rest. In Eq. (4), we neglect molecular diffusion of sediment because it is negligible when compared to the effects of turbulent transport. Applying a filter in the LES framework, denoted by the overbar, to Eqs. (2)–(4) gives

$$\frac{\partial \bar{u}_j}{\partial x_j} = 0, \tag{5}$$

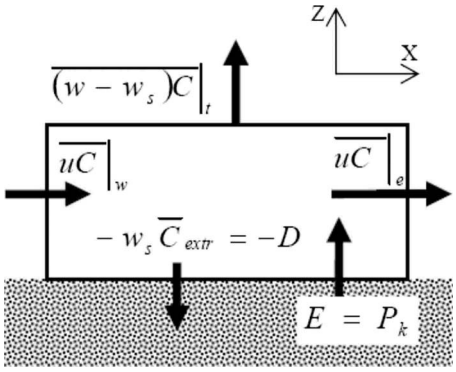

FIG. 1. A two-dimensional view in the x-z plane of sediment mass fluxes through a bottom cell. The y-direction fluxes are normal to the page.

$$\frac{\partial \bar{u}_i}{\partial t} + \frac{\partial(\overline{u_i u_j})}{\partial x_j} = -\frac{1}{\rho}\frac{\partial \bar{p}}{\partial x_j}\delta_{ij} + \nu\frac{\partial^2 \bar{u}_i}{\partial x_j \partial x_j}, \tag{6}$$

$$\frac{\partial \bar{C}}{\partial t} + \frac{\partial}{\partial x_j}(\overline{u_j C} - \overline{w_s \delta_{j3} C}) = 0. \tag{7}$$

Discretizing Eqs. (6) and (7) over a three-dimensional finite volume of length Δx, width Δy, and height Δz with flux faces in the x direction denoted by e (east) and w (west), the y direction denoted by s (south) and n (north), and the vertical direction denoted by t (top) and b (bottom) gives the discrete finite-volume form of the momentum equations,

$$\begin{aligned}\frac{d\bar{u}_i}{dt} &+ \frac{1}{\Delta x}\left[\left(\overline{u_i u} - \nu\frac{\partial \bar{u}_i}{\partial x}\right)_e - \left(\overline{u_i u} - \nu\frac{\partial \bar{u}_i}{\partial x}\right)_w\right] \\ &+ \frac{1}{\Delta y}\left[\left(\overline{u_i v} - \nu\frac{\partial \bar{u}_i}{\partial y}\right)_n - \left(\overline{u_i v} - \nu\frac{\partial \bar{u}_i}{\partial y}\right)_s\right] \\ &+ \frac{1}{\Delta z}\left[\left(\overline{u_i w} - \nu\frac{\partial \bar{u}_i}{\partial z}\right)_t - \left(\overline{u_i w} - \nu\frac{\partial \bar{u}_i}{\partial z}\right)_b\right] \\ &= -\frac{1}{\rho}\frac{\partial \bar{p}}{\partial x_i}\delta_{ij},\end{aligned} \tag{8}$$

where u, v, and w represent the velocity at cell faces in the x, y, and z directions, respectively. In a similar manner, the finite-volume form of the sediment transport equation is given by

$$\begin{aligned}\frac{d\bar{C}}{dt} &+ \frac{1}{\Delta x}(\overline{uC}|_e - \overline{uC}|_w) + \frac{1}{\Delta y}(\overline{vC}|_n - \overline{vC}|_s) \\ &+ \frac{1}{\Delta z}[\overline{(w-w_s)C}|_t - \overline{(w-w_s)C}|_b] = 0.\end{aligned} \tag{9}$$

From Eqs. (8) and (9), it can be seen that boundary conditions for either the x or the y direction are not needed if we enforce periodicity in the horizontal. As illustrated in Fig. 1, for bottom boundary conditions, denoted by the subscript "bed," assuming an immobile bed and employing a drag law for momentum gives

$$\left(\nu\frac{\partial \bar{u}_{1,2}}{\partial z} - \overline{u_{1,2}w}\right)_{\text{bed}} = C_D U \bar{u}_{1,2}, \tag{10}$$

$$\left(\nu\frac{\partial \bar{u}_3}{\partial z} - \overline{u_3 w}\right)_{\text{bed}} = 0, \tag{11}$$

and for the sediment,

$$\overline{(w-w_s)C}|_{\text{bed}} = \overline{wC}|_{\text{bed}} - w_s\bar{C}|_{\text{bed}} = E - D, \tag{12}$$

where C_D is the drag coefficient, $U=\sqrt{\bar{u}_1^2+\bar{u}_2^2}$, D represents sediment deposition, and E represents erosion. The sediment deposition term D is calculated with $w_s\bar{C}_{\text{extr}}$, where $\bar{C}_{\text{extr}}$ represents the near-bed sediment concentration and can be obtained via extrapolation from interior points as in Ref. 24. In the following numerical example, a quadratic extrapolation that uses three interior points along the z direction is employed. Sediment erosion is modeled through the use of the pickup function P_k as

$$\overline{wC}|_b = E = P_k, \tag{13}$$

which implies that sediment entrainment from the bed results from all turbulent near-bed fluxes rather than just the turbulent diffusive flux, as implied by Eq. (1). In this formulation, there is no restriction on the magnitude of the eddy viscosity. Furthermore, since we have not applied any specific turbulence model in the above derivation, the formulation in Eq. (13) is applicable to any turbulence model since all turbulent fluxes are parametrized by the pickup function P_k. This can be seen if we rewrite the finite-volume form of the sediment equation at the bed but substitute the fluxes above the bed to obtain (ignoring the y-direction flux)

$$\begin{aligned}\frac{d\bar{C}}{dt} &+ \frac{1}{\Delta x}(\overline{uC}|_e - \overline{uC}|_w) + \frac{1}{\Delta z}\overline{(w-w_s)C}|_{\text{bed+1}} \\ &= \frac{1}{\Delta z}[P_k - w_s\bar{C}_{\text{extr}}],\end{aligned} \tag{14}$$

which shows that a turbulence model only needs to be implemented to compute the terms on the faces above the bed ($\overline{wC}_{\text{bed+1}}$, $\overline{uC}|_e$, and $\overline{uC}|_w$) and not specifically at the bed.

III. LARGE-EDDY SIMULATION

A. Subgrid-scale model for the suspended sediment and the numerical method

In this paper we employ LES to calculate the transport of suspended sediment in strongly turbulent flow [Re $=O(600\,000)$] and use the computational code for solving the momentum and scalar transport equations that was developed by Zang *et al.*[25] and parallelized by Cui and Street,[26] which employs the DMM for the SFS motions. In this code, a finite-volume method is used to discretize the governing equations on a nonstaggered grid. All the spatial derivatives except the convective terms are discretized with second-order central differences. The convective terms in the momentum equation are discretized using a variation of quadratic upstream interpolation for convective kinematics,[27] and the convective terms for scalar transport are discretized using SHARP (simple high-accuracy resolution program),[28] which is third-order spatially accurate. In order to ensure stability near the bottom where strong sediment concentra-

tions exist, first-order upwinding is used in the bottom-most five cells. The second-order accurate Crank–Nicholson scheme is used for temporal discretization of the viscous terms, and the second-order accurate Adams–Bashforth scheme is used for all other terms. The momentum equation is advanced with a predictor-corrector procedure based on the fractional-step method, which calculates the velocity field at each time step by correcting the predicted velocity with the pressure gradient. This code has been successfully applied to the simulation of numerous laboratory-scale flows, including turbulent lid-driven cavity flow,[25] coastal upwelling,[26,29] breaking interfacial waves,[30] and sediment transport.[12,13] In this section we summarize the turbulence model for the suspended sediment and the associated boundary condition derived in Sec. II. The derivation of the turbulence model for the momentum equations is analogous to that for the suspended sediment, and details can be found in Ref. 23.

In LES, we apply a spatial filter to the equation governing the transport of suspended sediment [Eq. (7)] to obtain

$$\frac{\partial \bar{C}}{\partial t} + \frac{\partial}{\partial x_j}[(\bar{u}_j - w_s\delta_{j3})\bar{C}] = -\frac{\partial \chi_j}{\partial x_j}, \tag{15}$$

where the SFS flux χ_j is defined as

$$\chi_j = \overline{u_j C} - \bar{u}_j\bar{C}, \tag{16}$$

and we note (as described in Sec. III B) that the implementation of the bottom boundary condition in Sec. II does not require that we evaluate χ_3 at the bed. In DMM, χ_j is given by

$$\chi_j = -k_T\frac{\partial \bar{C}}{\partial x_j} + \overline{\bar{u}_j\bar{C}} - \bar{\bar{u}}_j\bar{\bar{C}}. \tag{17}$$

The first term on the right-hand side of Eq. (17) is an eddy-diffusivity model for the unresolved SFS flux, and the scalar diffusivity k_T is obtained with

$$k_T = \nu_T/\mathrm{Pr}_T, \tag{18}$$

where ν_T is the eddy viscosity and Pr_T is the turbulent Prandtl number. In this study, $1/\mathrm{Pr}_T$ is obtained dynamically following the procedure by Germano *et al.*[31] The resolved flux on the right-hand side of Eq. (17) consists of the second and third terms, which comprise the modified Leonard term (L_{ij}^m),

$$L_{ij}^m = \overline{\bar{u}_j\bar{C}} - \bar{\bar{u}}_j\bar{\bar{C}}. \tag{19}$$

Because of the explicit calculation of the modified Leonard term and the requirement to model only the residual stresses and fluxes, DMM requires "less" modeling. Furthermore, since Pr_T is determined dynamically, it does not require an empirical prescription.

B. Implementation of the pickup function as the bottom boundary condition

As a result of the finite-volume implementation at the bottom boundary, we do not need to evaluate χ_3 at the bed but instead must evaluate P_k. In dilute sediment transport in which particle-fluid interactions are neglected, sediment pickup is mainly a function of flow and particle properties, and the pickup function reads[32]

$$\frac{P_k}{\sqrt{(s-1)gd_0}} = \begin{cases} \alpha D^{*\beta}T^{*\gamma}, & \theta > \theta_c, \\ 0, & \text{otherwise}, \end{cases} \tag{20}$$

where α, β, and γ are constant coefficients to be determined, ρ_s is the sediment density, s is the specific weight of sediment, g is the gravitational acceleration, d_0 is the sediment diameter, the nondimensional diameter $D^* = d_0[(s-1)g/\nu^2]^{1/3}$, $T^* = (\theta-\theta_c)/\theta_c$, the Shields parameter θ is given by

$$\theta = \frac{\tau_b}{(s-1)\rho g d_0}, \tag{21}$$

and θ_c is the critical Shields parameter. The shear stress τ_b at the bottom is calculated with

$$\frac{\tau_b}{\rho} = C_D U_{\tan}^2, \tag{22}$$

where $U_{\tan} = \sqrt{\bar{u}_1^2 + \bar{u}_2^2}$ is the magnitude of the velocity component tangential to the channel bed, u_1 and u_2 are velocity components in the x and y directions, respectively, and C_D is the drag coefficient on the bottom. Based on the log law in the turbulent boundary layer, C_D is determined with

$$C_D = \left[\frac{1}{\kappa}\ln\left(\frac{z_1 + z_0}{z_0}\right)\right]^{-2}, \tag{23}$$

where $\kappa = 0.41$ is the von Karman constant, $z_0 = d_0$ is chosen to be the bottom roughness following Zedler and Street,[13] and $z_1 = 0.0022$ m is the distance between the channel bed and the center of the bottom-most cell. In the present study, we use the values $\alpha = 0.000\,33$, $\beta = 0.3$, and $\gamma = 1.5$ in Eq. (20) as suggested by van Rijn[32] from experimental data.

As shown above, rather than using reference concentrations, which are determined from the equilibrium state, the pickup function is employed as the bottom boundary condition for the SFS flux of sediment. As described by Eqs. (20)–(22), the sediment entrainment at the bottom boundary is directly related to the instantaneous local shear stress, which enables simulation of sediment transport in unsteady flows.

C. Near-wall model

In order to resolve fine near-bottom sediment and velocity gradients, the near-bottom vertical resolution must be refined. However, this results in high-aspect-ratio, pancake-shaped grid cells near the bottom and leads to problems in the LES formulation. First, in the presence of the pancake-shaped grid cells, where the vertical grid spacing is much smaller than the horizontal grid spacing, the eddies may be well resolved in the vertical but not so in the horizontal, thus

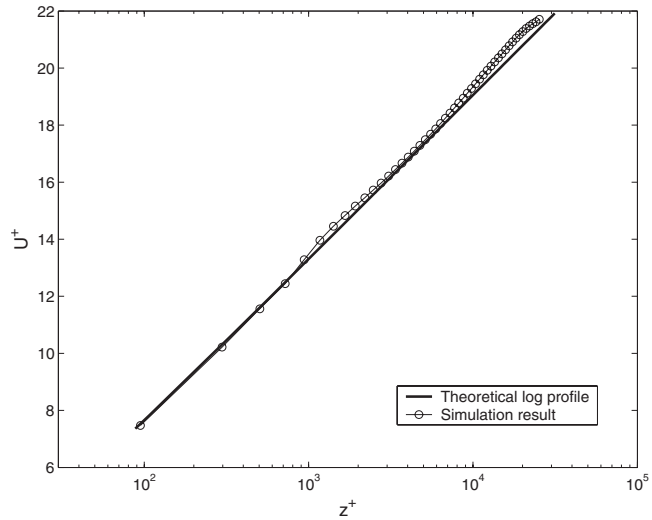

FIG. 2. The normalized vertical profile of the spatiotemporally averaged streamwise velocity after reaching the statistically steady state, along with an analytical log profile. The Reynolds number is roughly 600 000 based on the channel depth, and the labels represent plus units, i.e., $z^+=zu_*/\nu$, $U^+=\langle\bar{\bar{u}}\rangle/u_*$, where $\bar{\bar{u}}$ is defined in Eq. (27), and $\langle\ \rangle$ is the temporal average.

introducing errors. Scotti *et al.*[33] examined the dynamic Smagorinsky model in the context of high-aspect-ratio grids. They found that for such grids, higher-wavenumber modes do not have access to all the local triadic interactions and as a result the eddies experience a high drain of energy. Their modification of the eddy-viscosity model based on the grid aspect ratio did not compensate for this behavior. Second, the filtering process and the physical existence of the subgrid roughness alter the distribution of stresses near the wall. By filtering the flow field in a direct numerical simulation (DNS) of flow over a wavy boundary, Nakayama and Sakio[34] and Nakamaya *et al.*[35] found that the filtered near-wall velocities in the LES domain are apparently only influenced by the large wavelength topography but that the small wavelength roughness elements in the original DNS boundary generate stress near the new, smoothed boundary. Very near the rough wall, then, the flow physics, the grid aspect ratio, and the effect of filtering require special treatment in the turbulence model.

To account for the effects of the pancake-shaped near-wall grid in this study, following the work of Chow *et al.*,[36] we implement a near-wall model for momentum by augmenting the shear stress with

$$\tau_{i,\text{near wall}} = -\int C_c a(z) U \bar{u}_i dz, \tag{24}$$

where $i=1,2$, C_c is a scaling factor related to the grid aspect ratio (Fig. 13 in Ref. 36), and $a(z)$ (m^{-1}), a function allowing the smooth decay of the forcing function as the cutoff height h_c is approached, is set to $\cos^2(\pi z/h_c)$ for $z<h_c$ and zero otherwise. As proposed in the context of other boundary layer flow simulations,[35,37,38] the form of Eq. (24) is physically and mathematically reasonable. Employing this near-wall treatment with the present turbulence model gives us a satisfactory log profile of the streamwise velocity (see Fig. 2). Furthermore, a resolution study is presented in the Appendix, which shows that the current simulation code along with the wall model used in the present study gives the same log profile for different temporal and spatial resolutions.

D. Simulation parameters

The simulations in this study are performed in a rectangular channel of size $2\times1\times0.6$ m^3 $(L\times W\times H)$ with $128\times64\times48$ grid cells, which results in grid sizes of $\Delta x=\Delta y=0.0156$ m and $0.0045\leq\Delta z\leq0.0264$ m due to the stretching ratio $\Delta z_{k+1}/\Delta z_k=1.05$. Flow is forced with a constant pressure gradient, which yields a maximum streamwise velocity of $\bar{u}_{\max}\approx1$ m s^{-1}, yielding a Reynolds number based on the channel depth of 600 000, where $\nu=10^{-6}$ m^2 s^{-1}. The lateral boundaries are periodic, the top boundary is a free-slip rigid-lid boundary, and a drag law is implemented at the bottom, as described in Sec. II. The suspended sediment grain size is $d_0=100$ μm and the sediment density is $\rho_s=2650$ kg m^{-3}, which yields a settling velocity of $w_s=7.8\times10^{-3}$ m s^{-1}. In order to generate turbulence, the flow field is initialized with a theoretical log profile in the streamwise direction and random perturbations in all three velocity components. The theoretical log profile is given by

$$\bar{u} = \frac{u_*}{\kappa}\ln\frac{z+z_0}{z_0}, \tag{25}$$

where $u_*=\sqrt{-H\partial p/\partial x}=0.0490$ m s^{-1}. Using Eqs. (22) and (23), the temporally- and spatially-averaged value of the friction velocity after the flow reaches statistically steady state is slightly smaller and is $u_*=0.0431$ m s^{-1}. We use this smaller value of u_* in the present paper since it accounts for the effects of the near-wall shear stress augmentation model, which acts as an additional momentum sink. After the flowfield reaches a statistically-steady state, the maximum free-stream velocity $U_{\max}\approx1$ m s^{-1}, and the sediment is initialized with a uniform concentration field after the flowfield reaches a statistically-steady state. Time in the present results is normalized by the flowthrough time (T_F) defined by $T_F\equiv L/U_{\max}=2$ s. Physical quantities are normalized by scaling parameters listed in Table I. In what follows, all times are relative to the start of the sediment calculations after the velocity field has come to statistical equilibrium. The simulation time step is 0.005 s, and the Courant–Friedrich–Levi number (CFL$=u\Delta t/\Delta x$) is roughly 0.40.

IV. RESULTS AND DISCUSSION

A. Temporal variability

Figure 3 depicts the temporal evolution of the laterally averaged normalized concentration profiles and contours during the period $0\leq t/T_F\leq37.5$. The laterally averaged concentration is given by

$$\hat{\bar{C}}(x,z,t) = \frac{1}{W}\int_0^W \bar{C}(x,y,z,t)dy. \tag{26}$$

As depicted in Figs. 3(a)–3(d), sediment is picked up from the bed at the start of the simulation and forms an interface between the sediment-water mixture and the clear water that rises to the top boundary. This fast-moving interface indi-

TABLE I. Scaling parameters used to normalize physical quantities.

Scale	Parameter
Time	$T_F = L/U_{\max}$ (flowthrough time)
Velocity	u_*
Inner vertical length scale	$\delta = \nu/u_*$
Outer vertical length scale	H
Streamwise length scale	L
Spanwise length scale	W
Concentration	$\langle \tilde{\bar{C}}_a \rangle = \frac{1}{700T_F}\int_{200T_F}^{900T_F}\frac{1}{LW}\int_0^W\int_0^L \bar{C}(x,y,z=0.007\ \text{m},t)dxdydt$
Flux	$w_s\langle \tilde{\bar{C}}_a \rangle$

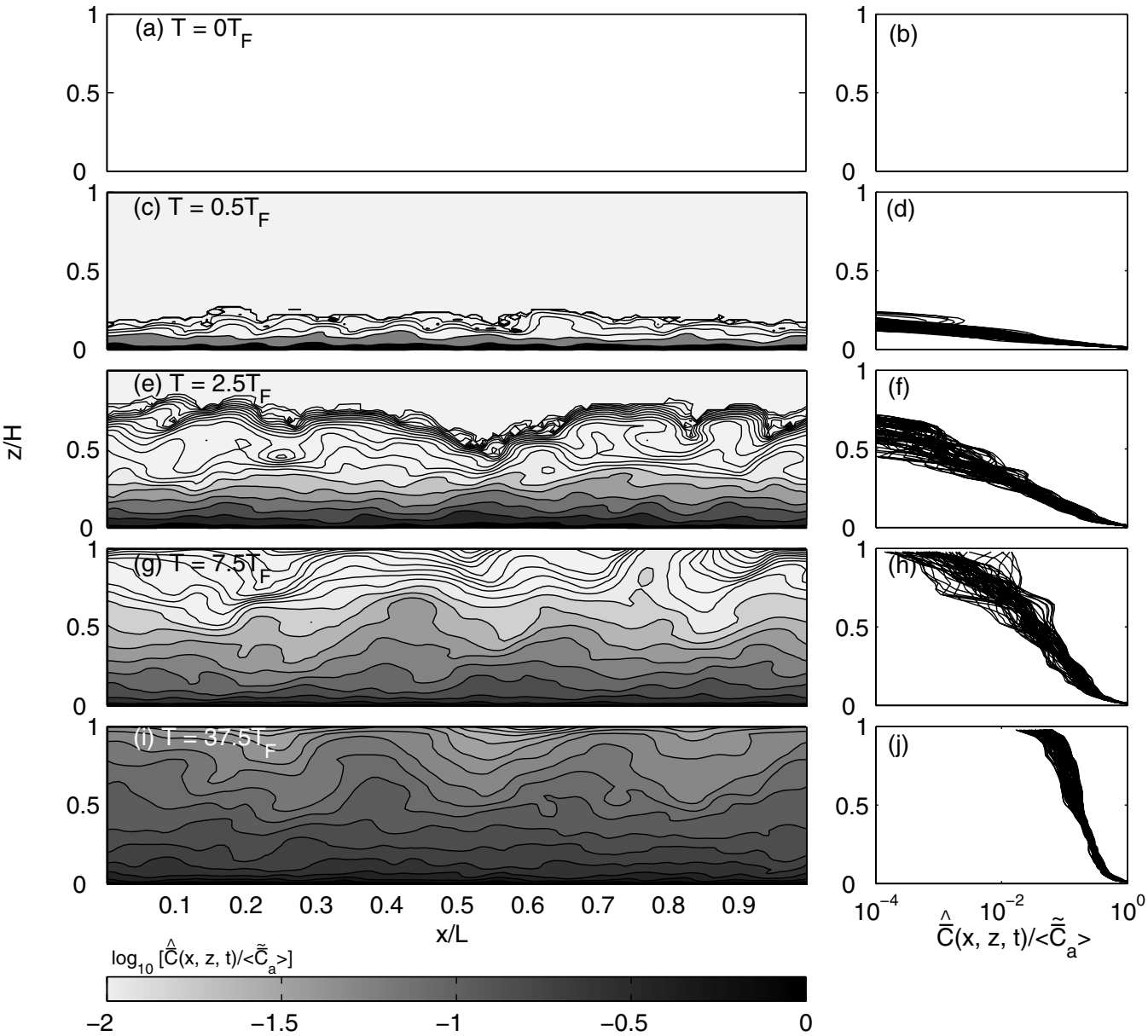

FIG. 3. The temporal evolution of the laterally averaged normalized concentration, $\hat{\bar{C}}/\langle \tilde{\bar{C}}_a \rangle$, contours [(a), (c), (e), (g), and (i)], and profiles [(b), (d), (f), (h), and (j)]. In (d), (f), (h), and (j) each line represents a normalized concentration profile at different streamwise (x) locations along the channel.

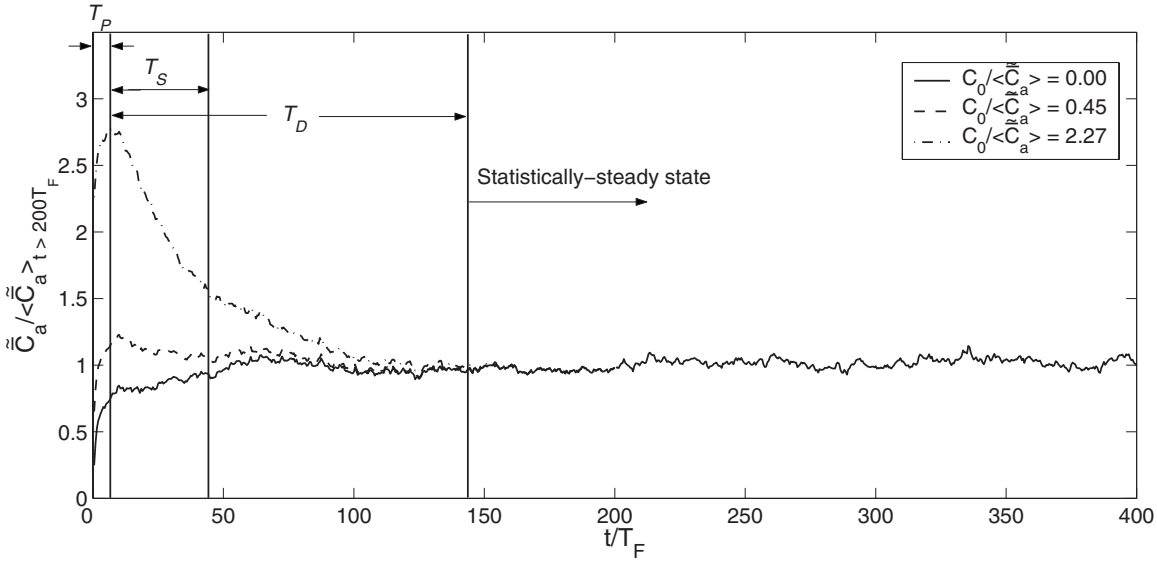

FIG. 4. Time histories of the normalized planform-averaged reference concentration $\tilde{\tilde{C}}_a/\langle\tilde{\tilde{C}}_a\rangle$ for three different initial conditions showing the time scales associated with the transient behavior of the suspended sediment concentration. To highlight the transient nature of the flow, here we only show the period $0 \le t \le 400T_F$, although we run the simulations for a total of $900T_F$.

cates that the suspended sediment spreads over the channel depth very rapidly because of vertical mixing, as shown in Figs. 3(c)–3(f). Due to the strong gradient and strong turbulence at the rising concentration interface [Figs. 3(c) and 3(e)], the behavior of sediment suspension during this time period is dominated by turbulent mixing. This process persists until the concentration interface reaches the domain top, as in Fig. 3(f). Using the friction velocity $u_* = 0.0431\ \text{m s}^{-1}$, the time scale of this initial period can be approximated by $T_P = H/u_* \approx 7T_F$, which represents the time scale over which the sediment that is picked up at the start of the simulation is distributed over the entire water column. As shown in Figs. 3(e)–3(h), once the sediment–clear water interface reaches the top boundary, the no-flux boundary condition prevents continued upward flux of sediment and downward flux due to settling begins to counteract the upward flux due to turbulent diffusion.

After the initial pickup period T_P, the sediment concentration field continues to transition until it comes to statistical equilibrium at $t \approx 200T_F$. The dynamics of this transitional period can be examined by investigating the temporal variation of the planform-averaged suspended sediment concentration at a fixed height above the bed, which is given by

$$\tilde{\tilde{C}}(z,t) = \frac{1}{LW}\int_0^L \int_0^W \bar{C}(x,y,z,t)dxdy. \tag{27}$$

Figure 4 shows the time history of the planform-averaged reference concentration $\tilde{\tilde{C}}_a$ normalized by a temporally averaged value, $\langle\tilde{\tilde{C}}_a\rangle$ (see Table I). In order to illustrate different time scales and to compare the effects of different initial conditions, simulations are performed using three different initial conditions of uniform sediment concentration $\bar{C}_0$, namely, $\bar{C}_0/\langle\tilde{\tilde{C}}_a\rangle = 0$, $\bar{C}_0/\langle\tilde{\tilde{C}}_a\rangle = 0.45$, and $\bar{C}_0/\langle\tilde{\tilde{C}}_a\rangle = 2.27$. All three results are plotted together in Fig. 4. In addition to the rapidly fluctuating turbulent time scale, there are other time scales that are evident in the transient behavior of the suspended sediment. As in Fig. 3, the first short time scale T_P is associated with the rapid response of the sediment pickup. This time scale is evident in the time series for all three initial conditions because the flux of sediment near the bed is so large that it overwhelms any variability associated with changing initial conditions.

To examine the other time scales in Fig. 4, we first introduce the simplified nondimensional sediment transport equation,

$$\frac{\partial \bar{C}}{\partial t'} = \frac{\partial}{\partial z'}\left(\frac{T}{T_S}w_s\bar{C} + \frac{T}{T_D}k_T'\frac{\partial \bar{C}}{\partial z'}\right), \tag{28}$$

where $t' = t/T$, $z' = z/H$, T is the dominant time scale, H is the depth, and $k_T' = k_T/\hat{k}_T$ is the nondimensional scalar diffusivity, which has been nondimensionalized with the depth-averaged scalar-diffusivity obtained by assuming a parabolic eddy-viscosity law such that

$$\hat{k}_T = \frac{\nu_T}{\text{Pr}_T} = \frac{1}{H}\int_0^H \frac{1}{\text{Pr}_T}z\left(1 - \frac{z - z_0}{H - z_0}\right)dz. \tag{29}$$

Using $\text{Pr}_T = 1.4$, as demonstrated in Sec. IV C, this gives $\hat{k}_T = 0.0013\ \text{m}^2\ \text{s}^{-1}$. In Eq. (28) we have modeled all turbulent motions (resolved and unresolved) as a vertical gradient-diffusion process using an eddy viscosity. Turbulent transport of sediment is thus dominated by two important terms, namely, sediment settling, which has a time scale of $T_S = H/w_s = 38.5T_F$, and turbulent mixing, which has a time scale of $T_D = H^2/\hat{k}_T = 135T_F$. The settling time scale T_S is the time it takes sediment to fall through the entire water column due to gravitational settling, which is evident for the cases in Fig. 4, which have nonzero initial sediment concentrations. Since turbulent mixing depends on the concentration gradi-

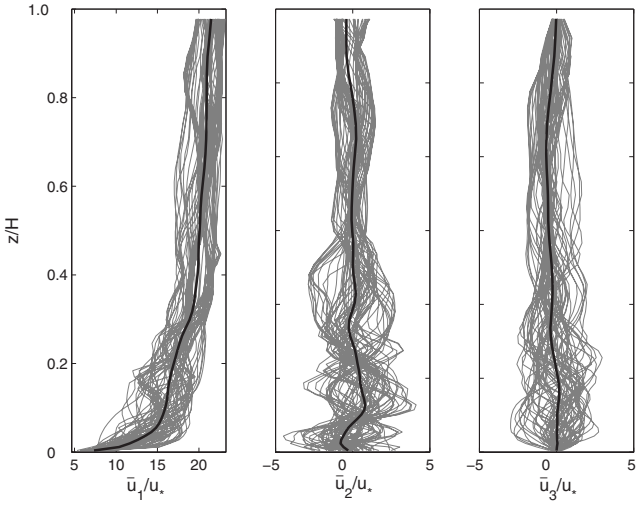

FIG. 5. Instantaneous (gray thin lines) along with normalized mean (black thick lines) velocity profiles of the streamwise component $\bar{u}_1$ (left), the spanwise component $\bar{u}_2$ (middle), and the vertical component $\bar{u}_3$, along the centerline of the channel every $0.015L$ as one moves downstream at $t=550T_F$. The black thick line in each component represents the mean value of gray thin lines.

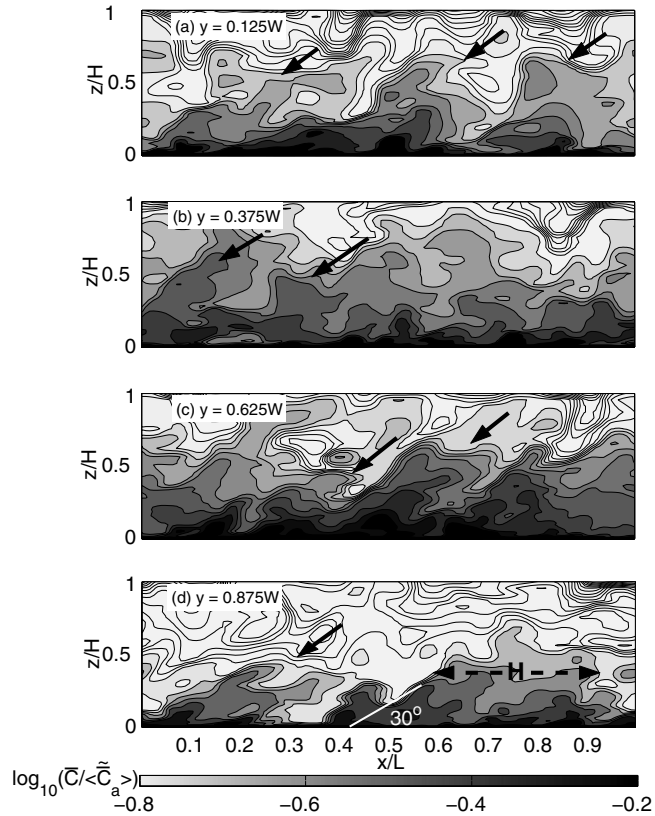

FIG. 6. Snapshots of the normalized concentration contours in four vertical planes along (a) $y=0.125W$, (b) $y=0.375W$, (c) $y=0.625W$, and (d) $y=0.875W$ at $t=550T_F$ showing the inclined angle and the length scale of the sediment bulge in (d). Sediment bulges are indicated by black solid arrows.

ent, at the start of the simulation when the concentration field is uniform, the gradient is so small that sediment settling is the dominant transport mechanism. This results in a significant drop in the sediment concentration for the cases in which $\bar{C}_0/\langle\tilde{\bar{C}}_a\rangle=0.45$ and $\bar{C}_0\langle\tilde{\bar{C}}_a\rangle=2.27$ during the period $T_P<t\leq T_P+T_S$ in Fig. 4, over which time the initial sediment field is settling onto the bed. During this settling period, the near-bed concentration decreases rapidly (particularly for $\bar{C}_0/\langle\tilde{\bar{C}}_a\rangle=2.27$) due to the downward flux of settling sediment. After $t\approx T_P+T_S=45.5T_F$, although most sediment has already deposited onto the bed, the difference between the three cases is still significant, indicating that the concentration field has not reached its statistically-steady state. Rather than a rapid downward flux due to settling (as is the case for the period $T_P<t\leq T_P+T_S$), the sediment concentration subsequently decreases more slowly until $t\approx T_P+T_D=142T_F$, at which time all three concentration signals are nearly identical, which is consistent with the idea that statistically-steady state is reached when the concentration field is independent of the initial sediment concentration field $\bar{C}_0$. The time period $T_P+T_S<t\leq T_P+T_D$ is that associated with the competition between the upward flux of sediment due to turbulent mixing and the downward flux due to settling. During this time period, sediment settling and turbulent mixing are equally important and the upward flux of sediment is slightly less than that due to settling, causing a relatively slow decrease in the near-bed concentration.

In summary, from the time series of the planform-averaged sediment concentration with three different initial conditions, three significant time scales, T_P, T_S, and T_D, can be found. The first time scale, $T_P=H/u_*$, can be seen as the turnover time scale of the most energetic eddies, which is the smallest flow time scale and only depends on the flow itself. The second time scale, $T_S=H/w_s$, is the settling time scale that only depends on the properties of the particles. The third time scale, $T_D=H^2/\hat{k}_T$, is a large time scale associated with turbulent mixing of sediment. Because turbulent mixing is due to velocity fluctuations that contain lower energy than that associated with the large eddies or gravitational settling, the turbulent mixing time scale is the longest of the three time scales discussed here.

B. Spatial variability

Figure 5 shows instantaneous and mean streamwise velocity profiles at $t=550T_F$ along the channel centerline. The figure shows that, at an instant in time, there is considerable spatial variability in each velocity component, and this spatial variability is greater near the bed. Due to the no-flux boundary condition, the vertical component of velocity ($\bar{w}$) vanishes at the bottom, whereas the y component ($\bar{v}$) persists. Deviations from the mean values are accompanied by significant spanwise and vertical velocity fluctuations, which enhance the local concentration of suspended sediment. The strong spatial variability of the concentration is shown in Fig. 6, which depicts the concentration contours in four vertical planes along $y=0.125W$, $0.375W$, $0.625W$, and $0.875W$ at $t=550T_F$. In the cases that sediment is not well-mixed in the vertical direction as in Figs. 6(a), 6(c), and 6(d), these concentration contours clearly show sediment bulges associated with large-scale turbulent features. Sediment bulges are coherent patches of sediment entrained into the flow by the turbulent eddies. They are distinguished by regions of high

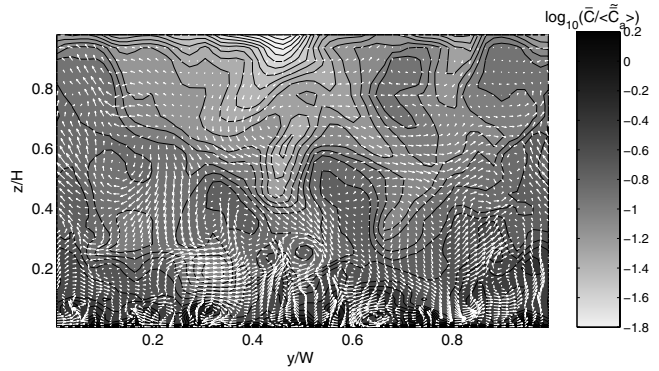

FIG. 7. Velocity vectors superimposed over the normalized concentration contours in a cross-sectional plane at $x=0.5L$ and $t=550T_F$.

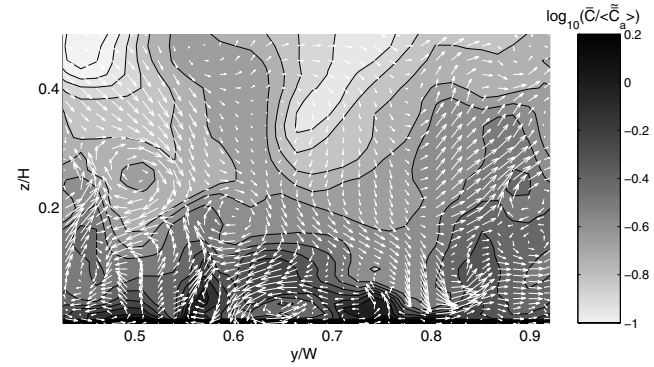

FIG. 8. A zoom-in plot of Fig. 7 in the region where high concentration is associated with strong near-bottom eddies and upward sediment flux.

sediment concentration relative to the surrounding flow, as indicated by the dark solid arrows in Fig. 6. In the present simulation, these sediment bulges are typically of the lengths of $0.5H \sim 1.5H$ in the streamwise direction and inclined at a characteristic angle of 30°. These properties have also been found to be characteristic of the large-scale turbulent features in the outer region of the turbulent boundary layer from laboratory experiments.[39,40]

In order to further investigate how sediment suspension is linked to the ambient flow field, in Fig. 7 we plot instantaneous concentration contours superimposed over the velocity vectors in a cross-sectional plane at $x=0.5L$. The figure shows transport of the suspended sediment associated with the resolved large eddies. Near the bottom, patches of high sediment concentration correspond to high eddy intensity or upward flux. These eddies form vortex cores and can extend downstream, thereby greatly enhancing sediment transport in the streamwise direction. As will be illustrated in Sec. IV C, the mean vertical sediment flux due to the eddy diffusion is much less than that induced by the resolved field. Therefore, the transport of suspended sediment in our results is mainly due to advection by the resolved turbulent eddies. Once sediment is mobilized by the excess shear stress, which we model with the pickup function, it is further entrained into the water column only if the ambient turbulent flux is strong enough to overcome the gravitational settling. Otherwise, suspended sediment will deposit at the bottom, and its motion will be dominated by granular forces. This eddy-transport phenomenon is illustrated further in Fig. 8, which depicts a zoom-in plot of Fig. 7. Figure 8 depicts high sediment concentration with weak spatial variability near the bed and suspension of sediment due to the strong, coherent eddies and upward velocity. These near-bottom vortex structures and the associated sediment transport were also found by Zedler and Street,[12,13] who simulated a high Reynolds number channel flow using LES with a different wall model and boundary conditions.

C. Spatiotemporally averaged sediment concentration

As shown in Fig. 4, statistically-steady state is reached at roughly $t=150T_F$ and occurs when the upward turbulent flux of sediment is balanced by the settling of sediment due to gravity. Figure 9 depicts the planform-averaged concentration profile $\tilde{\bar{C}}$ [Eq. (27)] that is also averaged over time from $t=200T_F$ to $900T_F$, and the result is compared to the Rouse curve, which, in the temporal-averaged and planform-averaged sense, is derived by assuming a parabolic eddy viscosity to yield[41]

$$\frac{\langle \tilde{\bar{C}} \rangle}{\langle \tilde{\bar{C}}_a \rangle} = \left(\frac{a}{H-a} \frac{H-z}{z} \right)^{\mathrm{Pr}_T w_s / \kappa u_*}, \tag{30}$$

where H is the water depth and Pr_T is the turbulent Prandtl number defined in Eq. (18). Typically, the Rouse profile given by Eq. (30) is used to describe the sediment concentration profile in steady, uniform open channel flows and is directly derived from the parabolic eddy diffusivity. It has been validated with laboratory observations in the limits of low concentration and small particle size (e.g., Refs. 42 and 43). Greimann and Holly, Jr.[44] state that the Rouse curve is valid for flows with low sediment concentration $\bar{C} < 0.1$ and small Stokes number $\mathrm{St}_b/(\kappa z/H) \ll 1$, where $\mathrm{St}_b = t_b u_*/H$ and the particle time constant t_b is estimated as $w_s \rho_s \bar{C}^{1.7}/[g(\rho_s - \rho)]$. For the present simulation, these condi-

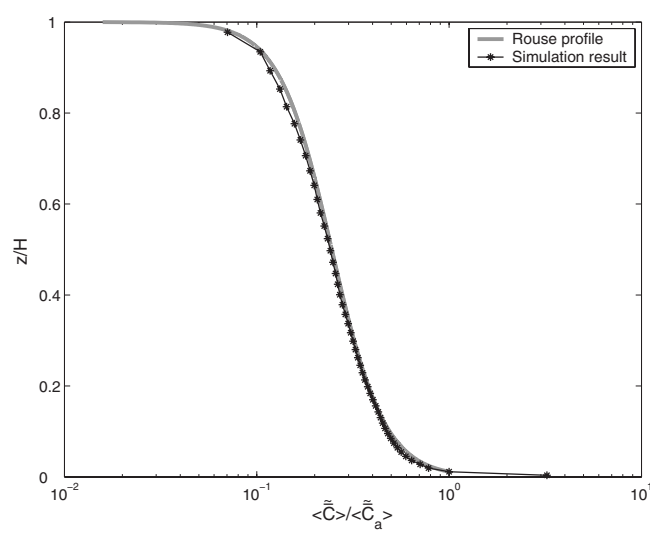

FIG. 9. The normalized spatiotemporally averaged concentration profile (the black solid line) and the Rouse curve (the gray thick line). The data are averaged every second over the period $200T_F \leq t \leq 900T_F$.

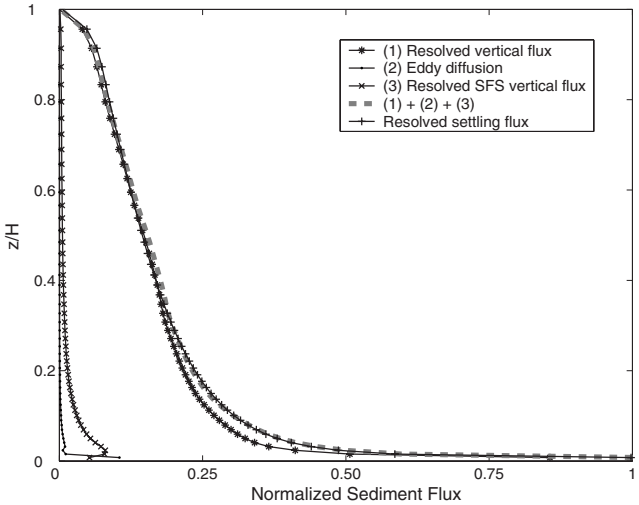

FIG. 10. Different components of the spatiotemporally averaged vertical fluxes normalized by $\langle \widetilde{w_s C_a} \rangle$ on a linear scale.

tions are satisfied with $\bar{C} < 0.01$ in most parts of the domain and $\mathrm{St}_b/(\kappa z/H) < 5 \times 10^{-4}$. The value of Pr_T in Eq. (30) varies with measurements obtained in different studies. By comparing to the data by Vanoni,[45] van Rijn[42] showed good agreement between the experimental data and Rouse curves, and Pr_T was thus empirically expressed as

$$\frac{1}{\mathrm{Pr}_T} = 1 + 2\left(\frac{w_s}{u_*}\right)^2. \tag{31}$$

In the book by Raudkivi,[43] a different set of data is presented for comparison with Rouse curves, and good agreement can also be found. Raudkivi[43] suggested that $1/\mathrm{Pr}_T \approx 1$ for fine sediment, whereas for coarse sediment $1/\mathrm{Pr}_T < 1$. By analyzing the equilibrium state with the finite mixing length approach, Nielsen and Teakle[46] showed that Pr_T is an increasing function of w_s/u_* and a decreasing function of the distance from the bed for a constant mixing length and is usually larger than 1. In the present study, we use $\mathrm{Pr}_T = 1.4$, which yields good agreement between simulation data and the Rouse profile and is consistent with the value suggested by experiments[42,43,45] and theory.[46] The von Karman constant κ in Eq. (30) can be reduced by 0.2% (Ref. 47) to 17% (Ref. 48) due to the influence of stratification, which can be particularly important for suspension of fine sand caused by large bed shear stress near the bed in the field.[49] However, owing to the negligible buoyancy effect of the fine sediments and the low concentration in most of the water column in this study, stratification is neglected and we set $\kappa = 0.41$, while the friction velocity is $u_* = 0.0431$ m s^{-1}, as described in Sec. III D. Given these parameters, comparison of Eq. (30) with the simulation result yields good agreement as shown in Fig. 9.

D. Components of the subfilter-scale stress

In order to analyze the physics of the SFS model, we compare the components of the SFS stress to understand which components contribute to most of the turbulent suspended sediment flux. In order to investigate this, we perform the spatiotemporal average, denoted by $\langle \tilde{\ } \rangle$, of the LES sediment transport Eq. (15) to obtain (at statistically-steady state)

$$\frac{\partial}{\partial x_3}\left[\left\langle \widetilde{k_T \frac{\partial \bar{C}}{\partial x_3}} \right\rangle - \langle \widetilde{\overline{\bar{u}_3 \bar{C}} - \bar{\bar{u}}_3 \bar{\bar{C}}} \rangle - \langle \widetilde{\bar{u}_3 \bar{C}} \rangle + \langle \widetilde{w_s \bar{C}} \rangle\right] = 0. \tag{32}$$

The terms in this expression represent the following:

$$\left\langle \widetilde{k_T \frac{\partial \bar{C}}{\partial x_3}} \right\rangle, \quad \text{eddy diffusion (unresolved SFS flux)},$$

$$\langle \widetilde{\overline{\bar{u}_3 \bar{C}} - \bar{\bar{u}}_3 \bar{\bar{C}}} \rangle, \quad \text{resolved SFS vertical flux},$$

$$\langle \widetilde{\bar{u}_3 \bar{C}} \rangle, \quad \text{resolved vertical flux},$$

$$\langle \widetilde{w_s \bar{C}} \rangle, \quad \text{resolved settling flux}.$$

These spatiotemporally averaged flux components are plotted on linear and log scales in Figs. 10 and 11, respectively. The figures show that most of the sediment flux is due to the resolved vertical and settling fluxes, which is to be expected for a sufficiently resolved LES. Closer to the bed, however, the resolved SFS flux becomes larger, and it is always one order of magnitude larger than the eddy-diffusive flux and is the main contributor to the SFS flux. One would expect a higher contribution from the eddy-diffusive flux on a coarser grid based on the relation between the eddy diffusivity and the grid size. Furthermore, one can see that at steady state, the summation of each vertical flux component due to the flow exactly balances the downward flux due to settling.

V. CONCLUSION

We have simulated the suspension of fine sediment in a high Reynolds number channel flow [$\mathrm{Re} = O(600\,000)$] using LES with a new boundary condition that eliminates problems associated with small near-bed eddy viscosities. To account for the SFS motions, we employ the DMM, which computes the resolved SFS motions with the Leonard term and the unresolved SFS motions with an eddy-viscosity model. Simulations show that, as expected for a sufficiently resolved LES, the resolved vertical sediment flux ($\langle \bar{u}_3 \bar{C} \rangle$) is one order of magnitude greater than the resolved SFS flux as computed by the Leonard term. The unresolved SFS flux, which is computed with the eddy-viscosity model, is in turn one order of magnitude smaller than that computed by the Leonard term in most of the water column.

The small magnitude of the eddy viscosity is typical for a well-resolved LES since the resolved SFS stress accounts for much of the SFS motions. As a result, modeling the sediment flux boundary condition at the bed with a turbulent

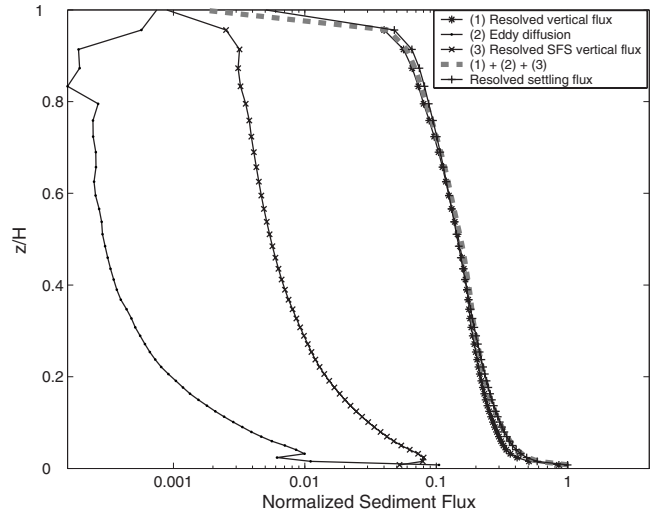

FIG. 11. Different components of the spatiotemporally averaged vertical fluxes normalized by $\langle \widetilde{w_s C_a} \rangle$ on a semilog scale.

diffusive flux can lead to unphysically large gradients in the near-bed sediment concentration that are required to offset the small-eddy viscosity. This boundary condition is ill posed because it ignores the fact that a significant portion of sediment flux from the bed consists of contributions from both the resolved flux of sediment and the resolved SFS flux (the Leonard term). Therefore, flux of sediment at the bed must include three terms, namely, the resolved flux, the resolved SFS flux (Leonard term), and the unresolved SFS flux (eddy-viscosity term), the sum of which is given by the filtered vertical flux of sediment ($\overline{u_3 C}$), and this total flux must be equal to the pickup function. Specification of the total flux as the boundary condition for erosion from the bed then enables a natural Dirichlet-type flux boundary condition at the bed using the finite-volume formulation, which requires a flux of sediment at the bottom face of the cell adjacent to the bed. In addition to eliminating problems associated with a small-eddy viscosity at the bed, this boundary condition does not require knowledge of the underlying turbulence model in order to model sediment erosion since the closure problem has been effectively eliminated via specification of $\overline{wC}$ (w is the vertical velocity at the cell face). Although specification of $\overline{wC}$ with the empirical pickup function may induce excessive sediment concentrations near the bed such that two- or three-way coupling methods may be required, we assume that these regions are small so that the assumption of one-way flow-sediment coupling is satisfactory and the present results are valid for dilute sediment transport in which the Eulerian method applies.

The simulation results illustrate interesting temporal variability during transition to statistically-steady state flow conditions. After being initialized with a uniform sediment concentration in a turbulent channel flow, the sediment transitions over three distinct periods, each with distinct time scales. First, the sediment field exhibits rapid response to the sediment pickup from the bed, leading to a rapid increase in the near-bed concentration until the sediment from the bed reaches the top boundary. The time scale of this transient period can be approximated by the pickup time scale $T_P = H/u_*$ where H is the depth and u_* is the shear velocity. After the initial pickup time scale, there is a subsequent transient period over which the settling and upward turbulent flux of sediment compete before coming into a statistically-steady balance. Initially, because the initial sediment field exhibits a weak concentration gradient, the dynamics is governed mostly by settling, and this occurs over an initial settling time scale $T_S = H/w_s$, where w_s is the settling velocity. As the sediment settles onto the bed, however, the near-bed sediment concentration gradient increases, resulting in an upward flux of sediment over a turbulent diffusive time scale $T_D = H^2/\hat{k}_T$, where $\hat{k}_T$ is the depth-averaged scalar diffusivity. The gravitational settling and turbulent mixing are equally important during this time period, resulting in a slow decrease in the near-bed concentration when the simulation is initialized with a nonzero concentration field. After this time period the upward turbulent flux and the downward flux due to settling are in statistical equilibrium, and the time series is independent of the initial sediment concentration field. During the statistically-steady state, the simulation results match the theoretically predicted Rouse curve.

The sediment concentration field also exhibits pronounced spatial variability that is tightly correlated with the resolved, energy-containing eddies. These eddies account for most of the resolved vertical flux of sediment and are clearly visible in streamwise and spanwise cross sections in the form of vortex cores. Although the near-bed sediment concentration is relatively high due to erosion, it is the spanwise vortices that act to eject near-bed sediment into the channel and contribute to most of the upward flux of sediment that balances the downward flux due to settling.

TABLE II. Simulation parameters for the resolution study.

Case	$N_X \times N_Y \times N_Z$	Δt (s)	Aspect ratio ($\Delta X/\Delta Z_{\min}$)	C_c in Eq. (24)
Base	$128 \times 64 \times 48$	0.005	7.8	0.75
Coarse	$128 \times 64 \times 32$	0.005	5.2	0.65
Fine	$128 \times 64 \times 64$	0.005	9.8	0.80
Smaller Δt	$128 \times 64 \times 48$	0.001	5.2	0.75

ACKNOWLEDGMENTS

We gratefully acknowledge the support of the ONR Coastal Geosciences Program under Grant No. N00014-05-1-0177 (Scientific officers: Dr. Tom Drake and Dr. Nathaniel Plant). We also thank Professor Bob Street for his extensive comments and suggestions that significantly improved the quality of this manuscript. We are grateful to the Stanford Center for Computational Earth and Environmental Science (CEES) for providing us with computational time on their Sun V20z Opteron Cluster and to the Army Research Laboratory Major Shared Resource Center for providing time on their LinuxNetworx Xeon EM64T cluster.

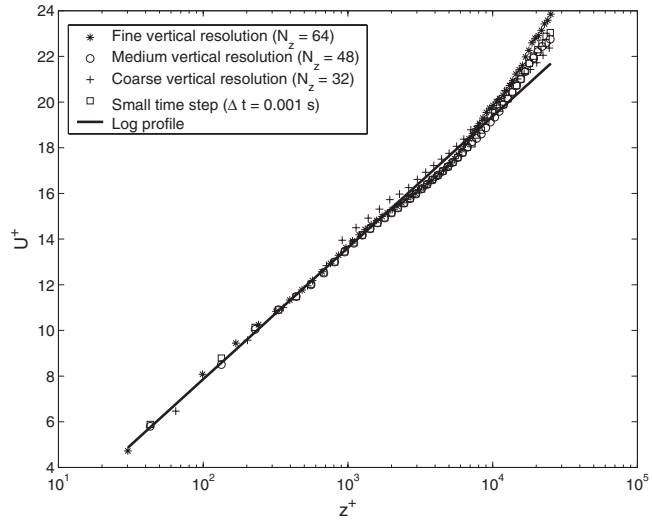

FIG. 12. The normalized vertical profiles of the spatiotemporally averaged streamwise velocity given by different spatial and temporal resolutions after reaching the statistically steady state, along with an analytical log profile.

APPENDIX: RESOLUTION STUDY

We performed a resolution study for the simulation code by employing three different vertical resolutions and two different temporal resolutions. As listed in Table II, the simulation with $128\times64\times48$ grid points and a time step of $\Delta t=0.005$ s represents the base case, and this is the same setup we use for the simulations in the present paper. The vertical grid resolutions with 32 and 64 grid points represent the coarse and fine vertical resolutions, respectively, and the simulation with a time step of $\Delta t=0.001$ s represents the simulation with a smaller time step. Due to grid stretching in the vertical, changing the vertical resolution leads to a change in the grid aspect ratio, which in turn requires a change in the scaling factor C_c in Eq. (24) for the wall model, as described in Sec. III C. Values for C_c are calculated using the formula of Chow *et al.*[36] and are listed in the last column of Table II. Other than differences in the vertical and temporal resolutions (and the value of C_c), simulation parameters are identical to those described in Sec. III D. The temporal average of the planform-averaged streamwise velocity is obtained during the period $100T_F\leq t\leq 200T_F$ (T_F is the flowthrough period), during which time the flow has reached a statistically steady state. Velocity profiles are plotted in the log-linear scale in Fig. 12, which shows that the present code yields nearly identical results for the different spatial and temporal resolutions employed.

[1] S. Pedinotti, G. Mariotti, and S. Banerjee, "Direct numerical simulation of particle flows in the wall region of turbulent flows in horizontal channels," Int. J. Multiphase Flow **18**, 927 (1992).
[2] S. Elghobashi and G. C. Truesdell, "On the two-way interaction between homogeneous turbulence and dispersed solid particles. I: Turbulence modification," Phys. Fluids A **5**, 1790 (1993).
[3] L. P. Wang and M. R. Maxey, "Settling velocity and concentration distribution of heavy particles in homogeneous isotropic turbulence," J. Fluid Mech. **256**, 27 (1993).
[4] C. Y. Yang and U. Lei, "The role of the turbulent scales in the settling velocity of heavy particles in homogeneous isotropic turbulence," J. Fluid Mech. **371**, 179 (1998).
[5] A. J. Dorgan and E. Loth, "Simulation of particles release near the wall in a turbulent boundary layer," Int. J. Multiphase Flow **30**, 649 (2004).
[6] T. Bosse, L. Kleiser, and E. Meiburg, "Small particles in homogeneous turbulence: Settling velocity enhancement by two-way coupling," Phys. Fluids **18**, 027102 (2006).
[7] T. G. Drake and J. Calantoni, "Discrete particle model for sheet flow sediment transport in the nearshore," J. Geophys. Res. **106**, 19859, DOI:10.1029/2000JC000611 (2001).
[8] Y. S. Chang and A. Scotti, "Entrainment and suspension of sediment into a turbulent flow over ripples," J. Turbul. **4**, 1 (2003).
[9] M. W. Schmeeckle and J. M. Nelson, "Direct numerical simulation of bedload transport using a local dynamic boundary condition," Sedimentology **50**, 279 (2003).
[10] J. Calantoni, T. Holland, and T. Drake, "Modelling sheet-flow sediment transport in wave-bottom boundary layers using discrete-element modelling," Philos. Trans. R. Soc. London, Ser. A **362**, 2985 (2004).
[11] W. Wu, W. Rodi, and T. Wenka, "3D numerical modeling of flow and sediment transport in open channels," J. Hydraul. Eng. **126**, 4 (2000).
[12] E. A. Zedler and R. L. Street, "Large-eddy simulation of sediment transport: Current over ripples," J. Hydraul. Eng. **127**, 444 (2001).
[13] E. A. Zedler and R. L. Street, "Sediment transport over ripples in oscillatory flow," J. Hydraul. Eng. **132**, 1 (2006).
[14] D. S. Byun and X. H. Wang, "The effect of sediment stratification on tidal dynamics and sediment transport pattern," J. Geophys. Res. **110**, C03011, DOI: 10.1029/2004JC002459 (2005).
[15] J. Young and A. Leeming, "A theory of particle deposition in turbulent pipe flow," J. Fluid Mech. **340**, 129 (1997).
[16] C. Villaret and A. G. Davies, "Modeling sediment-turbulent flow interactions," Appl. Mech. Rev. **48**, 601 (1995).
[17] J. D. Smith and S. E. McLean, "Spatially averaged flow over a wavy surface," J. Geophys. Res. **82**, 1735, DOI: 10.1029/JC082i012p01735 (1977).
[18] M. Garcia and G. Parker, "Entrainment of bed sediment into suspension," J. Hydraul. Eng. **117**, 414 (1991).
[19] J. A. Zyserman and J. Fredose, "Data analysis of bed concentration of suspended sediment," J. Hydraul. Eng. **120**, 1021 (1994).
[20] L. C. van Rijn, *Principles of Sediment Transport in Rivers, Estuaries and Coastal Seas* (Aqua, Amsterdam, the Netherlands, 1993).
[21] P. Nielsen, *Coastal Bottom Boundary Layers and Sediment Transport* (World Scientific, Singapore, 1992).
[22] L. C. van Rijn, "Applications of sediment pick-up functions," J. Hydraul. Eng. **112**, 867 (1986).
[23] Y. Zang, R. L. Street, and J. R. Koseff, "A dynamic mixed subgrid-scale model and its application to turbulent recirculating flows," Phys. Fluids A **5**, 3186 (1993).
[24] D. Gessler, B. Hall, M. Spasojevic, F. Holly, H. Pourtaheri, and N. Raphelt, "Application of 3D mobile bed, hydrodynamic model," J. Hydraul. Eng. **125**, 737 (1999).
[25] Y. Zang, R. L. Street, and J. R. Koseff, "A non-staggered grid, fractional step method for time-dependent incompressible Navier-Stokes equations in curvilinear coordinates," J. Comput. Phys. **114**, 18 (1994).
[26] A. Q. Cui and R. L. Street, "Large-eddy simulation of coastal upwelling flow," Environ. Fluid Mech. **4**, 197 (2004).
[27] B. P. Leonard, "A stable and accurate convective modelling procedure based on quadratic upstream interpolation," Comput. Methods Appl. Mech. Eng. **19**, 59 (1979).
[28] B. P. Leonard, "Simple high-accuracy resolution program for convective modelling of discontinuities," Int. J. Numer. Methods Fluids **8**, 1291 (1988).
[29] Y. Zang and R. L. Street, "Numerical simulation of coastal upwelling and interfacial instability of a rotational and stratified fluid," J. Fluid Mech. **305**, 47 (1995).
[30] O. B. Fringer and R. L. Street, "The dynamics of breaking progressive interfacial waves," J. Fluid Mech. **494**, 319 (2003).
[31] M. Germano, D. Piomelli, P. Moin, and W. H. Cabot, "A dynamic subgrid-scale eddy viscosity model," Phys. Fluids A **3**, 1760 (1991).
[32] L. C. van Rijn, "Sediment pick-up functions," J. Hydraul. Eng. **110**, 2494 (1984).
[33] A. Scotti, C. Meneveau, and M. Fatica, "Generalized Smagorinsky model for anisotropic grids," Phys. Fluids **9**, 1856 (1997).
[34] A. Nakayama and K. Sakio, "Simulation of flows over wavy rough boundaries," *Annual Research Briefs* (Center for Turbulence Research, NASA Ames-Stanford University, Stanford, CA, 2002), pp. 313–324.
[35] A. Nakayama, K. Hori, and R. L. Street, "Filtering and LES of flow over irregular rough boundary," in *Proceedings of the Summer Program* (Cen-

ter for Turbulence Research, NASA Ames-Stanford University, Stanford, CA, 2004), pp. 145–156.
[36]F. K. Chow, R. Street, M. Xue, and J. H. Ferziger, "Explicit filtering and resconstruction turbulence modeling for large-eddy simulation of neutral boundary layer flow," J. Atmos. Sci. **62**, 2058 (2005).
[37]A. R. Brown, J. M. Hobson, and N. Wood, "Large-eddy simulation of neutral turbulent flow over rough sinusoidal ridges," Boundary-Layer Meteorol. **98**, 411 (2001).
[38]R. T. Cederwall, "Large-eddy simulation of the evolving stable boundary layer over flat terrain," Ph.D. thesis, Stanford University, 2001.
[39]R. E. Falco, "Coherent motions in the outer region of turbulent boundary layers," Phys. Fluids **20**, S124 (1977).
[40]S. B. Pope, *Turbulent Flows* (Cambridge University Press, Cambridge, UK, 2001).
[41]H. Rouse, "Modern conceptions of the mechanics of turbulence," Trans. Am. Soc. Civ. Eng. **102**, 463 (1937).
[42]L. C. van Rijn, "Sediment transport. Part II. Suspended load transport," J. Hydraul. Eng. **110**, 1613 (1984).
[43]A. J. Raudkivi, *Loose Boundary Hydraulics* (A. A. Balkema, Rotterdam, the Netherlands, 1998).
[44]B. P. Greimann and F. M. Holly, Jr., "Two-phase flow analysis of concentration profiles," J. Hydraul. Eng. **127**, 753 (2001).
[45]V. A. Vanoni, "Transportation of suspended sediment by water," Trans. Am. Soc. Civ. Eng. **111**, 67 (1946).
[46]P. Nielsen and I. A. Teakle, "Turbulent diffusion of momentum and suspended particles: A finite-mixing length theory," Phys. Fluids **16**, 2342 (2004).
[47]X. K. Wang, Z. Y. Want, M. Z. Yu, and D. X. Li, "Velocity profile of sediment suspensions and comparison of log-law and wake law," J. Hydraul. Res. **39**, 211 (2001).
[48]J. K. Guo and P. Y. Julien, "Turbulent velocity profiles in sediment laden flows," J. Hydraul. Res. **39**, 11 (2001).
[49]R. L. Soulsby and B. L. S. A. Wainwright, "A criterion for the effect of suspended sediment on near-bottom velocity profiles," J. Hydraul. Res. **25**, 341 (1987).